

Article

Phase Transformation Crystallography in Pipeline HSLA Steel after TMCP

Mikhail L. Lobanov , Maria A. Zorina , Maxim S. Karabanalov, Nikolay V. Urtsev 
and Andrey A. Redikultsev

Heat Treatment & Physics of Metals Department, Ural Federal University, 19 Mira St., Ekaterinburg 620062, Russia; m.a.zorina@urfu.ru (M.A.Z.); m.s.karabanalov@urfu.ru (M.S.K.); n.urtsev@ausferr.ru (N.V.U.); a.a.redikultsev@urfu.ru (A.A.R.)

* Correspondence: m.l.lobanov@urfu.ru

Abstract: Thermo-mechanical controlled processing (TMCP) is employed to obtain the required level of mechanical properties of contemporary high-strength low-alloy (HSLA) steel plates utilized for gas and oil pipeline production. The strength, deformation behavior and resistance to the formation and propagation of running fractures of the pipeline steel are mainly determined by its microstructure and crystallographic texture. These are formed as a result of austenite deformation and consequent $\gamma \rightarrow \alpha$ -transformation. This present study analyses the crystallographic regularities of the structural and textural state formation in a steel plate that has been industrially produced by means of TMCP. The values of the mechanical properties that have been measured in different directions demonstrate the significance of the crystallographic texture in the deformation and failure of steel products. An electron backscatter diffraction (EBSD) method and crystallographic analysis were utilized to establish the connection between the main texture components of the deformed austenite and α -phase orientations. This paper demonstrates that the crystallographic texture that is formed due to a multipath $\gamma \rightarrow \alpha$ -transformation results from the α -phase nucleation on the special boundaries between grains with γ -phase orientations. The analysis of the spectra of the α - γ -interface boundary angle deviations from the Kurdjumov–Sachs (K–S), Nishiyama–Wassermann (N–W), and Greninger–Troiano (G–T) orientation relationships (ORs) allows to suggest that the observed austenite particles represent a secondary austenite (not retained) that precipitates at intercrystalline α -phase boundaries and correspond to the ORs with regard to only one adjacent crystallite.

Keywords: TMCP; HSLA steel; $\gamma \rightarrow \alpha$ -transformation; deformation anisotropy; EBSD; texture; orientation relationships



Citation: Lobanov, M.L.; Zorina, M.A.; Karabanalov, M.S.; Urtsev, N.V.; Redikultsev, A.A. Phase Transformation Crystallography in Pipeline HSLA Steel after TMCP. *Metals* **2023**, *13*, 1121. <https://doi.org/10.3390/met13061121>

Academic Editor: Joan-Josep Suñol

Received: 28 April 2023

Revised: 9 June 2023

Accepted: 13 June 2023

Published: 15 June 2023



Copyright: © 2023 by the authors. Licensee MDPI, Basel, Switzerland. This article is an open access article distributed under the terms and conditions of the Creative Commons Attribution (CC BY) license (<https://creativecommons.org/licenses/by/4.0/>).

1. Introduction

Contemporary HSLA steels and a specific industrial method of their processing that comprises controlled hot rolling and adjustable accelerated cooling (thermomechanical controlled processing—TMCP) are used to obtain the required combination of mechanical properties in steel plates designed for natural gas and crude oil pipeline production [1–4]. Increased resistance to the localization of plastic deformation and failure resistance are characteristic features of the pipeline products manufactured by means of TMCP. The mechanical and functional properties of high-strength pipeline steel (API-5L X70-X80 and above) are determined by its microstructure that predominantly consists of products of displacive phase transformation (primarily bainite), with an average grain size $\sim 1 \mu\text{m}$ [1].

The fine microstructure of steel plates forms during TMCP due to successive processes that include austenite deformation during hot rolling, which takes place almost without recrystallization at its final stages [5–7], and $\gamma \rightarrow \alpha$ -transformation during accelerated controlled cooling. The structure that is formed as a result of TMCP is characterized by a pronounced crystallographic texture [5,8–16]. According to [8,9] the texture of hot-rolled

steel is generally represented by main orientations from $\{100\}\langle 011\rangle$ to $\{211\}\langle 011\rangle$ and from $\{211\}\langle 011\rangle$ to $\{332\}\langle 113\rangle$. A study [10] determined the texture component fraction of pipeline steel (X100 strength grade) with a bainite and martensite structure after TMCP: $\{112\}\langle 110\rangle$, $\{223\}\langle 110\rangle$, $\{332\}\langle 113\rangle$ and $\{001\}\langle 110\rangle$. Other studies [11,13,17,18] have established that the main crystallographic texture components after the $\gamma \rightarrow \alpha$ -transformation are formed from the texture components of deformed or recrystallized austenite corresponding to the K–S, N–W ORs [19–23].

Studies [4,5,10–16,18,24] have pointed out the significance of crystallographic texture after TMCP in the formation of anisotropy of mechanical properties—foremost, ductility of a material that determines the level of resistance to the formation and propagation of the running fracture. More specifically, a study [10] demonstrated that the anisotropy of mechanical properties of steel plates is determined by $\{112\}\langle 110\rangle$ and $\{223\}\langle 110\rangle$ components. The strong ‘isotropic’ component $\{332\}\langle 113\rangle$ provides for a balanced combination of high strength and impact toughness.

Texture can affect steel strength and crack resistance in different ways, depending on the direction. Both theoretical calculations and experimental data provide reliable evidence that allow to conclude that the propagation of a brittle crack in α -Fe, i.e., in a metal material with a body-centered cubic (bcc) lattice, occur along $\{001\}$ crystallographic planes [14–16,24–26].

It is important to note that the crystallographic texture characterized by a relatively small number of components is formed as a result of $\gamma \rightarrow \alpha$ -transformation, which is a multi-path process that progresses according to ORs [11–13,27,28]. One austenite orientation can result in 12 (according to N–W ORs) or 24 (according to K–S or G–T ORs) ferrite orientations, as a result of phase transformation in steel and due to the absence of limitations for phase nucleation localization [29–33]. Therefore, the total number of the developed ferrite orientations within one γ -grain can be almost as high as $9 \times 12 = 108$ or $9 \times 24 = 216$ (where 9 is the number of stable deformation orientations of austenite, according to [29]). Twelve orientations of α -phase (4–6 in a packet) crystallites were observed in a study of bainite transformation [29] at 600 and 300 °C after warm rolling of a carbon medium-alloy pipeline steel. Almost all possible α -phase orientations (24 orientations in four packets) were observed [30] within austenite grains in a low-carbon low-alloy steel with ferrite and bainite structure after $\gamma \rightarrow \alpha$ -transformation. Singular bainite packets that contained 1–2 crystallographic orientations were only observed in the narrow strips that had formed between ferrite grains. Therefore, the development of all possible ferrite orientations in one parent austenite grain (or the minimal number ~6 that provides for stress relaxation during phase transformation) should lead to the development of an almost textureless state. However, all contemporary studies regarding the structure of HSLA after TMCP indicate that a pronounced texture that influences the finished product failure behavior is formed in the low-carbon low-alloy steel after TMCP [5,13,18]. The development of a limited number of orientations as a result of a multi-path $\gamma \rightarrow \alpha$ -phase transformation in a material with a complex structure suggests that there are several structural factors that significantly restrain the development of all possible orientations during phase transformation [28,29,34–36].

Several studies [15,26,37–39] have determined that the structure of low-carbon steel after TMCP contains fine, microstructurally non-homogenous regions with martensite and austenite (M-A constituent). It is assumed that some of the carbon enriches relatively small regions of the γ -solid solution and decreases its starting temperature of $\gamma \rightarrow \alpha$ -transformation. Therefore, the phase transformation in these regions is carried out at lower temperatures, last of all with partial austenite retention. The significance of the M-A regions as possible crack formation sites during HSLA steel fracture is pointed out in [15,26,39]. Within the scope of this present study, it is important to note that the structure of M-A regions that have partially undergone martensite transformation should most precisely characterize the crystallographic regularities of crystal lattice rearrangement during displacive transformations.

This present study is focused on the determination of the main crystallographic regularities of the phase transformations of hot-rolled austenite in HSLA steel that has undergone TMCP. The information regarding these crystallographic features, obtained as a result of this present study, should both broaden understanding of the transformation mechanisms of crystal lattices during polymorphic phase transformations and serve as a basis for the development of means of industrial material structure design during thermal and deformation processing in order to provide the specific combination of physical and mechanical properties of finished steel products.

2. Materials and Methods

This study was conducted on specimens of the HSLA steel that had undergone oxygen converter smelting (~0.05 Wt% C, ~1.5 Wt% Mn, ~0.2 Wt% Mo, ~0.05 Wt% Nb, the remainder comprising Fe and unavoidable impurities), designed for the production of X70 large diameter pipelines. The specimens were obtained from a plate that had undergone industrial TMCP.

A starting temperature of $\gamma \rightarrow \alpha$ -transformation ($A_3 \sim 840$ °C) was calculated from the chemical composition using Thermo-Calc-3 software (Thermo-Calc Software, Stockholm, Sweden). A_3 was estimated to lie in the range of 830–850 °C with the accuracy of the chemical element concentration measurement taken into account.

The industrial processing of the specimens was carried out with the finishing rolling temperature of ~880 °C. Therefore, the specimens underwent finishing hot rolling at the temperatures above the calculated A_3 , i.e., within a single γ -phase temperature range. The reduction percentages during the roughing and finishing passes of the hot rolling were ~57% and ~80%, respectively. The accelerated cooling was carried out after the hot rolling. The cooling rate of 25–40 °/s for different layers of the plate was calculated according to the method provided in [40].

The samples for specimen preparation were separated from the central region of the ~26–27 mm thick plate after TMCP. The integral texture of the plate that has a significant influence on the mechanical properties is best represented by the texture of the central region of the plate; therefore, the samples have undergone milling in the RD plane of the plate on both sides until their thickness reached 10 mm.

The separation of the samples for the investigation of mechanical property anisotropy was carried out along three directions: rolling direction (RD), transverse direction (TD) and at an angle of 45° to RD. Strain at the stage of necking was measured according to the method described in [4,41].

Tensile testing according to ASTM E8/E8M-21 was carried out on standard cylindrical specimens with a diameter of 5 mm and a gauge length of 25 mm on an Instron 3382 testing machine (Instron, High Wycombe, UK) at a 5 mm/min crosshead speed at room temperature.

Impact bending testing of the standard Charpy specimens (60 × 10 × 10 mm) was conducted using an Instron CEAST 9350 (Instron, High Wycombe, UK) drop tower impact system equipped with an environmental chamber, at an energy of 600 J, impact hammer starting speed of 3.7 m/s and temperature of –60 °C.

Scanning electron microscopy (SEM) was carried out on a ThermoScientific Scios 2 LoVac with an Oxford Instruments Symmetry EBSD Detector (Oxford Instruments, Abingdon, UK) at an accelerating voltage of 20 kV. Orientation estimation inaccuracy did not exceed $\pm 1^\circ$ ($\pm 0.6^\circ$ on average). The orientation maps (surface area ~40 × 40 μm^2 , scanning step = 25 nm) were used in order to establish the orientations of individual grains, as well as to conduct an analysis of the ORs and local crystallographic texture. The orientation maps (surface area ~1000 × 1000 μm^2 , scanning step = 1 μm) were used for the integral crystallographic texture analysis. The investigation of the integral texture was conducted utilizing the orientation distribution functions (ODF).

A coordinate system (X, Y, Z) with X—parallel to the RD, Y—parallel to the normal direction (ND) and Z—parallel to TD was used in both the structural studies and the textural analysis. The Z-axis also coincided with the normal to the surface of the metallographic

samples. Therefore, Z (TD) was the direction under investigation. In all figures presented in this paper that demonstrate an orientation study by means of EBSD (with the exception of the ODF), axes Y (ND), X (RD) and Z (TD) are directed vertically, horizontally and perpendicular to the plane of the figures, respectively.

The reconstruction of the high-temperature parent γ -phase was carried out using the AZtech Crystals software (Oxford Instruments, Abingdon, UK) according to the methods described in [42,43].

3. Results

Tensile and impact toughness tests were conducted in order to demonstrate the significance of the texture (both crystallographic and morphological) influence on the anisotropy of deformation and the failure of the steel that had undergone TMCP. The direction of testing affected the strength properties (YS and UTS) significantly; the influence was less significant for plastic properties (reduction area, total and uniform elongations) and impact toughness (KCV^{-60}), as shown in Table 1. The texture had the greatest impact on the behavior of deformation and failure at the necking stage of tensile testing (Figure 1). The fractures in specimens \parallel RD and \parallel TD acquired an ellipsoid shape (Figure 1a,b), which was more pronounced in the \parallel RD; the major ellipse axis was strictly parallel to the rolling plane. The fracture of the 45° RD specimen acquired a shape close to a circle (Figure 1c). Therefore, the texture provided for a relatively uniform deformation of all regions of the material at the failure stage.

Table 1. Results of the mechanical testing of steel after TMCP.

Specimen Separation Direction	YS/MPa	UTS/MPa	YS/UTS	Uniform Elongation/%	Total Elongation/%	Reduction Area /%	KCV^{-60} /J/cm ²
//RD	520 ± 10	630 ± 10	0.83	6.6 ± 0.4	20.3 ± 0.4	81.5 ± 0.5	280 ± 20
//TD	550 ± 10	670 ± 10	0.82	8.9 ± 0.5	23.5 ± 0.4	80.0 ± 0.5	260 ± 20
45°RD	500 ± 10	620 ± 10	0.81	7.5 ± 0.4	23.5 ± 0.4	84.5 ± 0.5	270 ± 20

YS—yield stress, UTS—ultimate tensile strength, KCV^{-60} —impact toughness at -60°C .

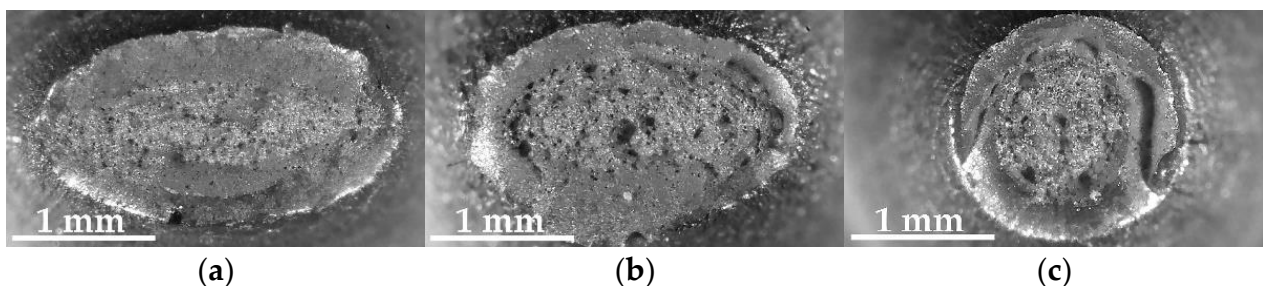


Figure 1. Fracture surfaces of the cylindrical specimens of HSLA steel after standard tensile testing: \parallel RD (a), \parallel TD (b), 45° RD (c).

Scanning electron microscopy revealed that the microstructure of the specimens (Figure 2) consists of different-sized non-equiaxial grains with dissected boundaries. Some of the grains (Figure 2a,b) can be consolidated into regions with smoothed boundaries. These regions extend in the RD and evidently represent the austenite grains (GB γ) that have been deformed during the hot rolling. The structure of the specimens also contains relatively fine regions (better visualized at a higher magnitude) of tempered martensite (Figure 2c,d) that appear to represent the M-A constituent [12,38,39]. It is also important to note that some regions contain fragments of the ferrite grains (Figure 2c,d), i.e., disperse polygons that appear to be separated by low-angle boundaries decorated with cementite precipitates. The average size of the α -phase grains in the studied specimen was determined to be $2.2 \pm 0.6 \mu\text{m}$ by means of orientation microscopy.

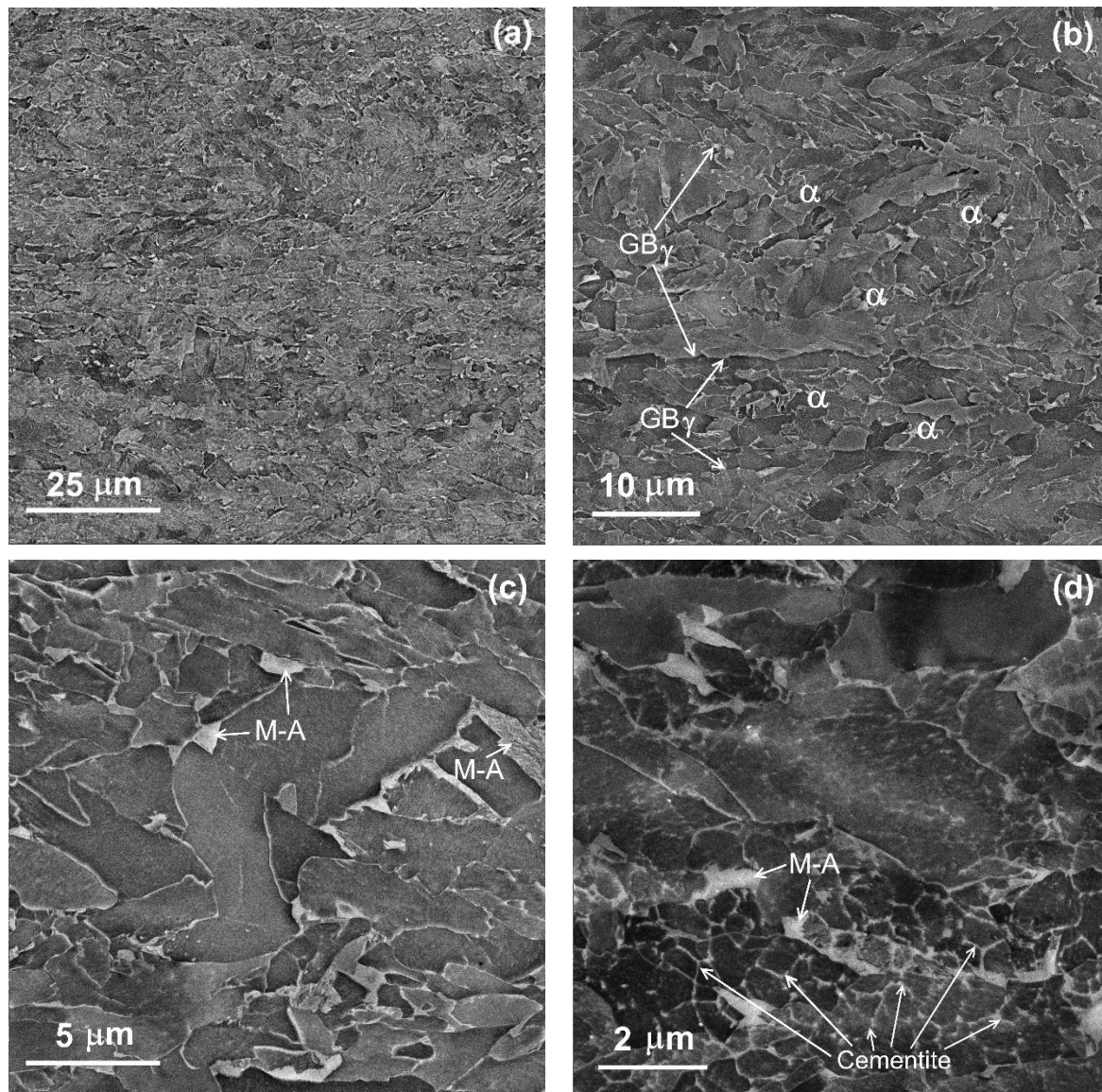


Figure 2. Microstructure of the specimen after TMCP (SEM, BSE-contrast): low magnification (a), the arrows indicate the boundaries of the initial austenite grains (GB_{γ}) (b), the arrows indicate the tempered martensite regions (M-A) (c), the arrows indicate the M-A constituents and cementite on the low-angle boundaries (d).

Orientation microscopy allows to observe a relatively pronounced texture: $\langle 111 \rangle$ and $\langle 100 \rangle$ crystallographic directions are parallel to ND and $\langle 112 \rangle$ and $\langle 110 \rangle$ directions are parallel to RD for the majority of the crystallites (Figure 3a,b).

The intercrystalline boundary spectra correspond to the structure obtained as a result of displacive phase transformations (Figure 3c,d) in accordance with the ORs, intermediate between the K-S and N-W ORs [12,34]. The majority of the high-angle boundaries lie within the range of the $47\text{--}60^\circ$ misorientation angles (Figure 3c,d). Within the special boundary spectrum of the α -phase $\Sigma 3$, $\Sigma 11$, $\Sigma 25b$ CSL-boundaries (coincidence site lattice) are predominant; a small number of $\Sigma 7$, $\Sigma 9$, $\Sigma 17b$, $\Sigma 29b$, $\Sigma 31b$, $\Sigma 33c$, $\Sigma 39b$, $\Sigma 41c$, $\Sigma 43c$, $\Sigma 45c$ CSL-boundaries can also be observed. The $\Sigma 3$, $\Sigma 11$, $\Sigma 25b$, $\Sigma 33c$, $\Sigma 41c$ boundaries have been formed during the $\gamma \rightarrow \alpha$ displacive transformation [12]. The presence of the rest of the boundaries is connected with the beginning of the relaxation processes (polygonization, primary recrystallization) in the bcc-lattice, according to the analysis conducted in [34]. The structures obtained by TMCP are evidently bainite with inclusions of tempered martensite.

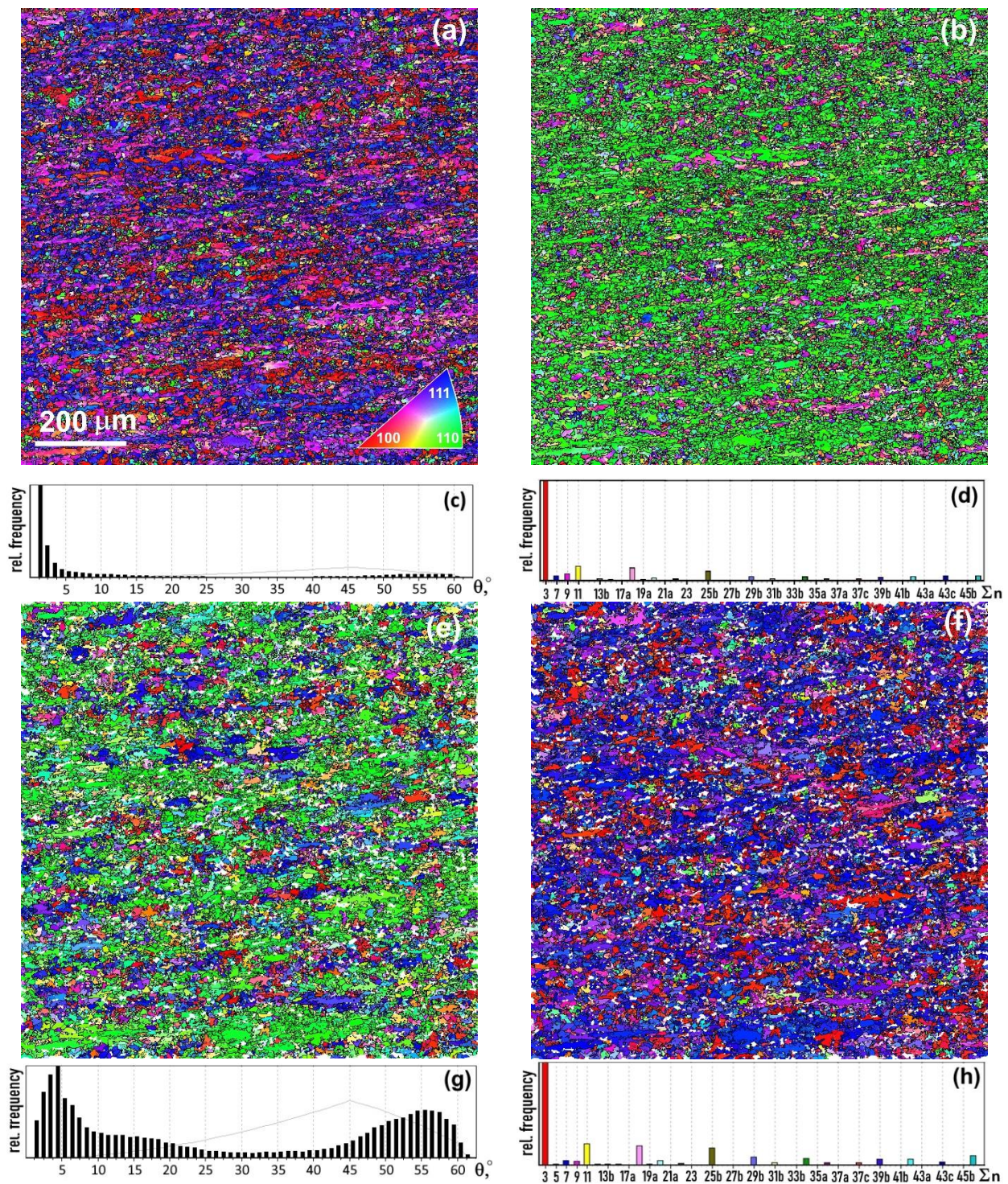


Figure 3. Macro-texture after TMCP (a–d) and reconstructed austenite grains (e–h): orientation maps in ND (a,e); orientation maps in RD (b,f); distribution of the boundary misorientation angles (c,g); and distribution of the CSL-boundaries (d,h).

The reconstructed austenite structure is also characterized by a well-pronounced texture (as indicated by the colouring). The main directions parallel to ND are $\langle 110 \rangle$ and $\langle 111 \rangle$; the prevailing direction parallel to RD is $\langle 111 \rangle$, but the $\langle 112 \rangle$ and $\langle 100 \rangle$ directions are also of note (Figure 3e,f).

The γ -phase spectrum of special boundaries after data reconstruction regarding austenite contains mostly $\Sigma 3$, $\Sigma 11$, $\Sigma 17b$, $\Sigma 25b$, $\Sigma 33c$, $\Sigma 41$, $\Sigma 45c$ CSL-boundaries that correspond to the texture after deformation of the face-centered cubic (fcc) metal [44].

A detailed analysis of the crystallographic texture (Figure 4) of the specimens reveals that the integral texture after TMCP is comprised of a range of scattered and, therefore, overlapping components: $\{001\}\langle 110\rangle$, $\{113\}\langle 110\rangle$ - $\{112\}\langle 110\rangle$, $\{223\}\langle 252\rangle$, $\{332\}\langle 113\rangle$ and $\{332\}\langle 023\rangle$. Two orientations close to $\{112\}\langle 110\rangle$ demonstrate the intensity that greatly exceeds that of the other orientations. These two orientations are mutually connected by the $\Sigma 3$ CSL misorientation (twins). These findings coincide with the TMCP texture presented in [4,8,12–16].

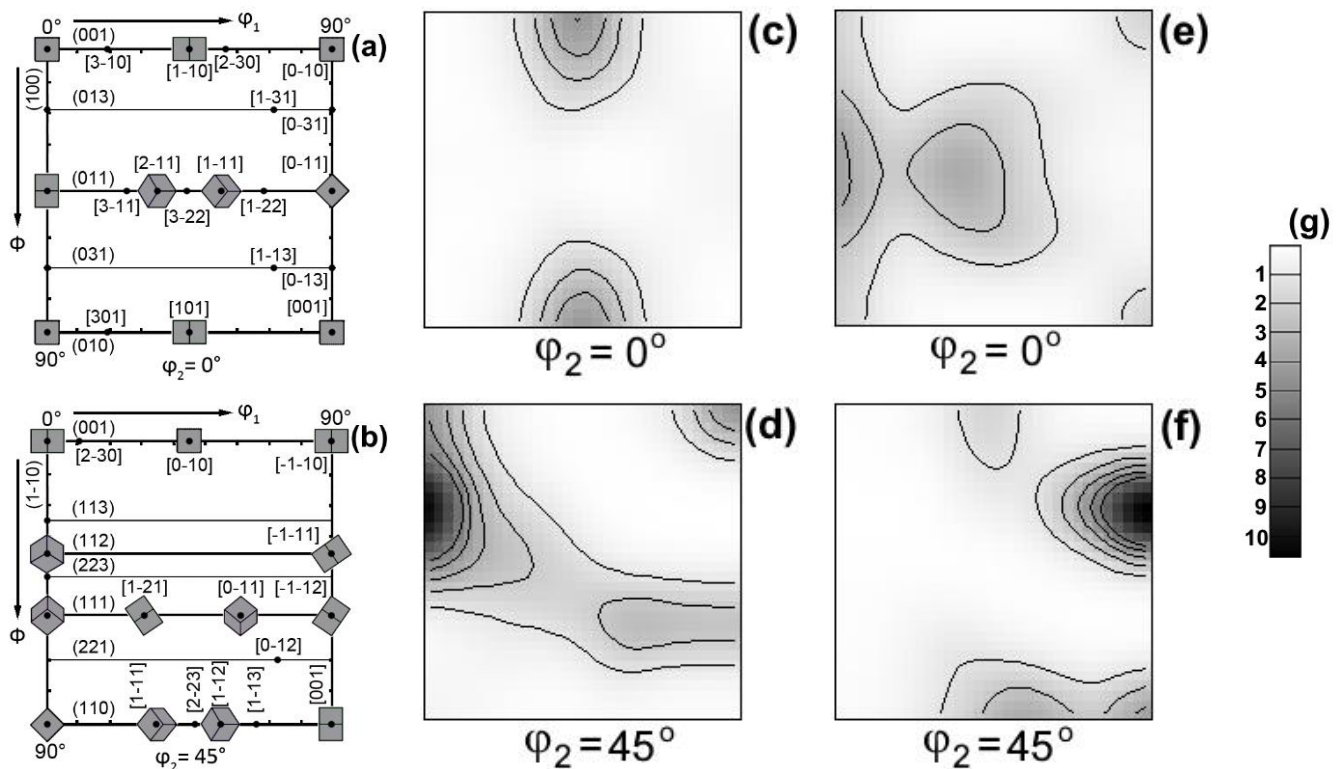


Figure 4. ODF cross-sections for $\phi_2 = 0^\circ$ and $\phi_2 = 45^\circ$ after TMCP (c,d); reconstructed austenite (e,f); standard ODF cross-sections (a,b); and the intensity scale (g).

It is important to note that the most intensive $\{112\}\langle 110\rangle$ orientations contain $\{100\}$ planes (cleavage planes in the bcc-lattice), which are located in the greatest proximity ($\sim 10^\circ$ deviation) to the geometrical planes of pipe fractures that form and propagate during ground tests of trunk pipelines [45], i.e., the planes that contain the pipe axis (that coincides with RD) and is inclined at 45° to the rolling plane.

The texture of the reconstructed γ -phase (Figure 3e,f) consists of the $\{113\}\langle 332\rangle$ - $\{112\}\langle 111\rangle$, $\{001\}\langle 001\rangle$, $\{110\}\langle 112\rangle$ and $\{110\}\langle 001\rangle$ components. Two orientations close to $\{112\}\langle 111\rangle$ demonstrate the intensity that greatly exceeds that of the other orientations. These two orientations are mutually connected by the $\Sigma 3$ CSL misorientation (twins). It is noteworthy that the reconstructed orientations coincide (strong) or are close to (weak) the stable deformation orientations of fcc steel that are formed during hot rolling [17,46]. A pronounced crystallographic directionality of the γ - α -transformation, i.e., a definite crystallographic orientation of the majority of the α -phase grains, should be noted. This directionality is triggered by the initial austenite grain orientations, with a significant variability of possible orientations that can develop during phase transformations that proceed according to K-S, N-W, G-T and other ORs. A significant intensity increase of $\{112\}\langle 110\rangle$ orientations is a result of the nucleation of the α -phase grains on the special

boundaries [13,16,28,34,47–49] that are formed between the grains of the matrix phase main orientations.

According to [47,49,50], α -phase nucleation should take place on the γ -phase boundaries with angle misorientations from the entire range of the possible angles between α -phase orientations that are formed in accordance with the ORs (N–W, K–S, G–T and others). Nucleation of a new phase on the $\Sigma 3$ CSL-boundaries of the γ -phase is fully consistent with this mechanism. These types of grain boundaries are predominant within the misorientation spectrum of the possible α -phase orientations (Figure 3d). The $\gamma \rightarrow \alpha$ -transformation on the coherent twin boundaries limits the range of the possible ORs that are determined by the stressed state during the course of the γ - α -transformation, grain orientation and boundary plane. This limits the number of new α -phase orientations, which leads to the formation of the α -phase texture (when texture is present in the γ -phase). The presence of boundaries with special properties in the γ -phase structure, e.g., special boundaries in the CSL-model [51,52], may determine the directionality and intensity of the phase transformations in steel [11]. This results in a crystallographic texture formation in the austenite decomposition products connected with the γ -phase texture.

Therefore, the formation of the nuclei of a new phase on the special (close to $\Sigma 3$) intergranular boundaries of the initial phase was established to be the main reason for the limitation of the multi-path nature of transformation. These boundaries form between the grains of the parent phase that are characterized by stable orientations obtained as a result of deformation, i.e., a pronounced directed treatment of steel.

Note that the crystallographic texture, formed by the rolling of the fcc-lattice with its consequent displacive transformation into the bcc-lattice, almost perfectly coincides with the texture of the bcc-lattice rolling.

The orientation investigation conducted on a smaller scale confirms (Figure 5) the regularities established above (Figures 3 and 4). The major α - and γ -phase orientations are practically repeated (Figure 5a,b,e,f) and the CSL-boundary spectra are reproduced (Figure 5d,h). In addition, it becomes evident that the grid of grain boundaries decorated with a carbon containing phase (Figure 2d) is represented by low-angle boundaries that confine the regions, the majority of which contain an increased dislocation density (Figure 5a,b). The latter is evidence of their displacive (not polygonizational) origin. The orientation studies at this level provide the identification of the largest γ -phase precipitates and their orientation connection with adjacent α -crystallites (Figures 6 and 7).

The interphase orientation analysis reveals that the spectra of the α - γ -interface boundary angle deviations from ORs are discrete. Only a minority of γ -phase precipitates are in the ORs with α -crystallites similar to K–S (4.5 – 5.5° at most, Figure 6b). Additionally, pronounced peaks at the angles close to 9.5 – 10.5° , 16.5 – 23.5° and 31.5 – 34.5° , and the most intensive at 42.5° are present within the spectra of the α - γ -interface boundary angle deviations from K–S ORs (Figure 6b).

The peak at the 42.5° angle corresponds to such a case when the orientations of the adjacent crystallites are nearly identical (Figures 6a and 7a), which is evidently erroneous, as it cannot occur during $\gamma \rightarrow \alpha$ -transformations that proceed according to any ORs (K–S, N–W and G–T). The absence of special misorientations between α - and γ -phase crystallites leads to a deviation from a precise OR at a constant angle ($\sim 42^\circ$) that corresponds to the minimal misorientation described by ORs. Such a situation can be attributed to an error in phase identification using OP-EBSD that is connected with the inaccuracies in the Hough transform [53].

A further interphase misorientation analysis was conducted by a ‘manual’ removal of the wrongly identified points from the orientation maps. Only the blurred peaks at low angles ($< 6^\circ$) and at angles close to 10° and 20° were registered within the spectra of the α - γ -interface boundary angle deviations from the K–S ORs following the additional error cleaning procedure. It is noteworthy that the $\gamma \rightarrow \alpha$ -phase transformation during TMCP proceeded in accordance with the ORs close to G–T (Figure 6e).

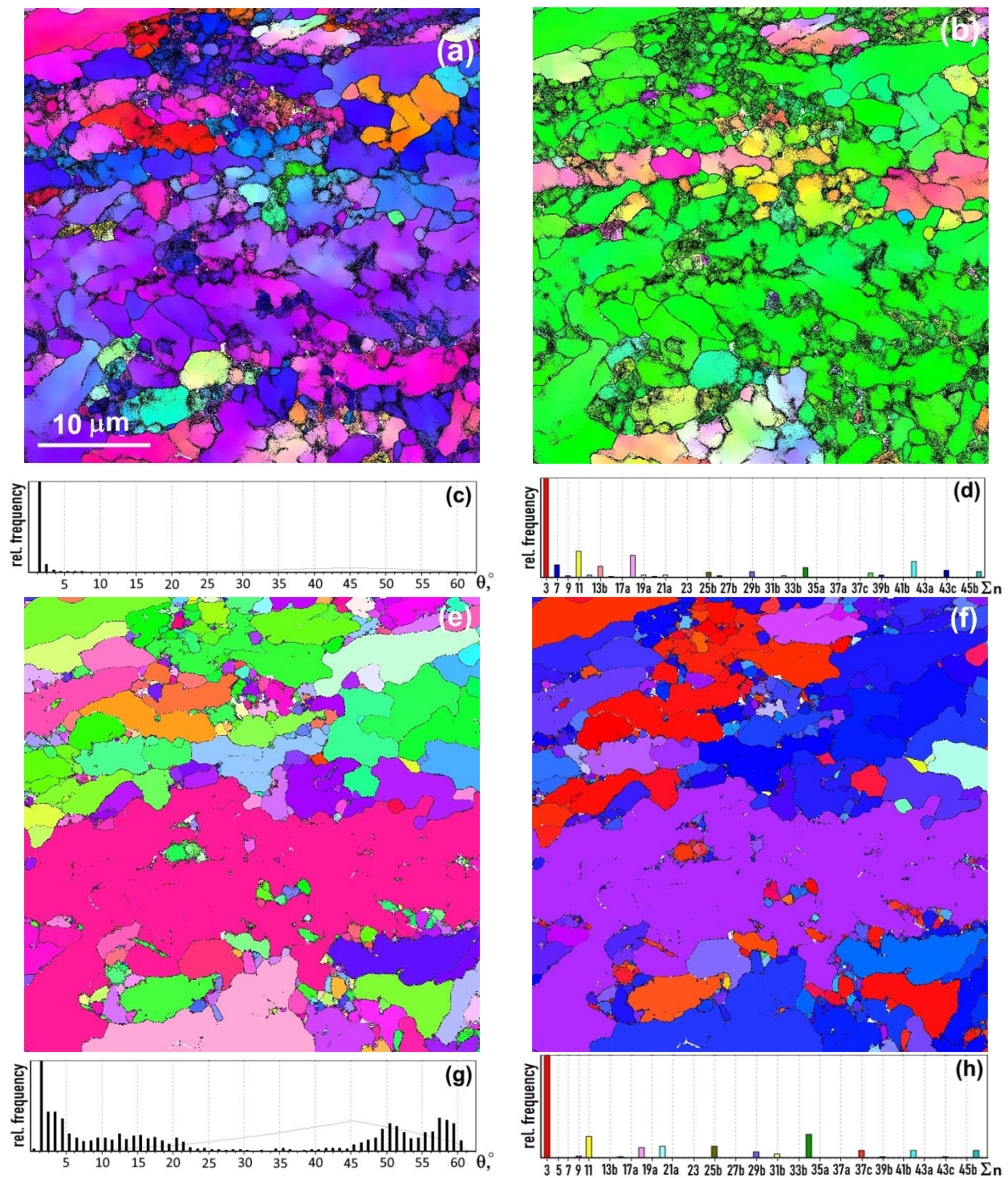


Figure 5. Micro-texture after TMCP (a–d) and reconstructed austenite grains (e–h): orientation maps in ND (a,e); orientation maps in RD (b,f); distribution of the boundary misorientation angles (c,g); and distribution of the CSL-boundaries (d,h).

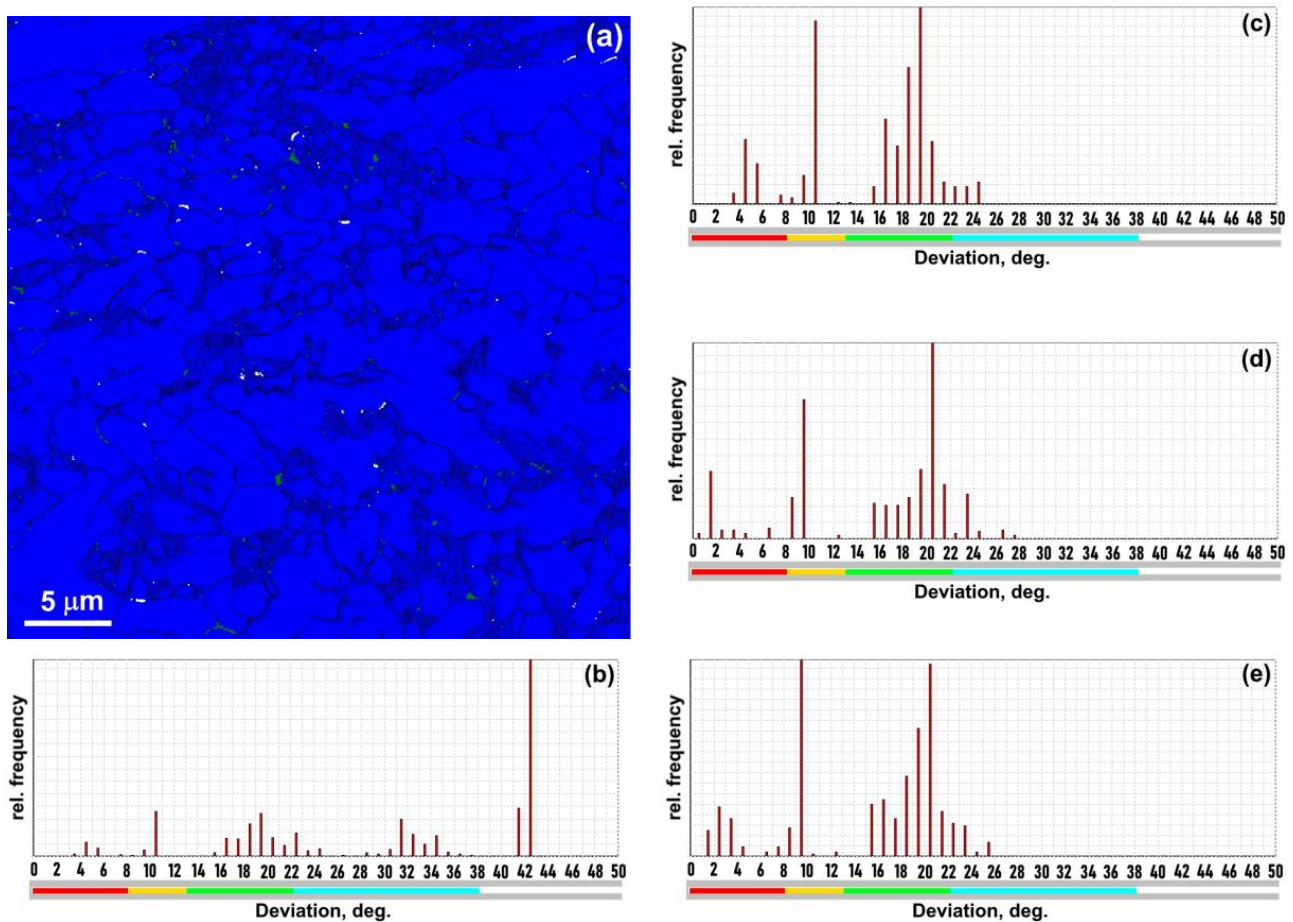


Figure 6. Phase map with the α -phase – blue, γ -phase – white, the boundaries between the α -crystallites misorientated at the $2\text{--}10^\circ$ angles – thin black lines, the boundaries between the α -crystallites misorientated at the angles above 10° – thick black lines (a); K–S before error cleaning of maps (b); K–S after error cleaning of maps (c); N–W after error cleaning of maps (d); and G–T after error cleaning of maps (e).

The types of spectra of α - γ -interface boundary angle deviations from any ORs can be explained by suggesting that the γ -phase particles are not austenite retained during a polymorphic transformation. These particles are secondary precipitates that are formed over the course of an $\alpha \rightarrow \gamma_{II}$ -transformation within a single austenite grain, whereby the transformation progresses on the ferrite crystallite boundary, but in accordance with ORs with regard to only one adjacent crystallite (Figure 7b–d). In order to test this hypothesis according to methods described in [28,49], all of the possible γ - and α -phase orientations that form during the γ -transformation were calculated: (1 orientation) $\rightarrow \alpha$ (24 orientations in accordance with K–S, G–T ORs and 12 orientations in accordance with N–W ORs) $\rightarrow \gamma_{II}$ (24×24 orientations in accordance with K–S, G–T ORs or 12×12 orientations in accordance with N–W ORs). This was followed by the analysis of all possible misorientations between all α - and γ_{II} -phase orientations.

The calculations revealed that the experimentally obtained deviations from the ORs at angles close to 10° and 20° ($\pm 2^\circ$) also corresponded to ORs. These misorientation angles should be observed between the α -grains that have been formed during the direct $\gamma \rightarrow \alpha$ -transformation and the γ_{II} -phase crystallites that have precipitated during the reverse $\alpha \rightarrow \gamma_{II}$ -transformation. In other words, these misorientations fulfill ORs (K–S, N–W and G–T), however, they have been formed as a result of austenite contacting with α -phase crystallites that are not connected to austenite by an initial OR. This austenite is a newly

formed secondary austenite, as its orientation differs from that of the parent austenite grain, within which it has been formed.

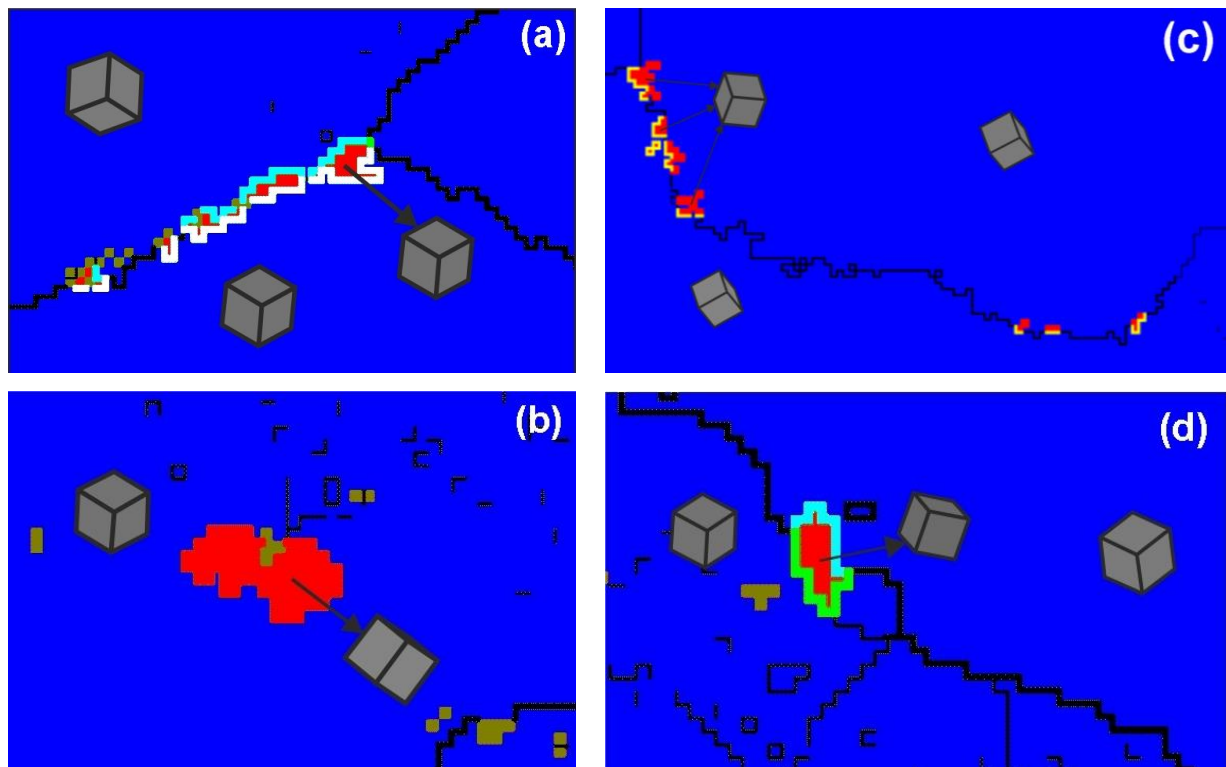


Figure 7. Phase map regions with austenite precipitates; interphase boundaries are coloured according to the fulfillment of the K-S ORs (Figure 6c): (a)—erroneous orientation, $\sim 42^\circ$ deviation from K-S ORs; (b)—up to 10° deviation from K-S ORs; (c)—austenite precipitate on a low-angle boundary—up to 10° deviation from K-S ORs on one side of the boundary and up to 20° deviation on the other side; and (d)—austenite precipitate on a high-angle boundary—up to 20° deviation from K-S ORs on one side of the boundary and up to 24° deviation on the other side.

The problem of retained (preserved) or secondary (newly occurred austenite) is key in understanding the mechanisms of phase transformations in steels, including their kinetics (shear, diffusion or diffusion-controlled shear), which cannot be fully resolved within the framework of this single study due to the lack of experimental material and errors in determining the orientations associated with the Hough transform. We believe that it can be resolved only within the framework of establishing crystallographic relationships between the phases, by which the microstructure and chemical composition are fixed by the final heat treatment. The present experimental equipment is capable of solving this task. Previously in [54,55], based on the crystallographic relationships between the phases at different cooling rates, we have established that the β -phase observed at room temperature for Ti-6Al-4V and Zr-2.5%Nb alloys is secondary with respect to the high-temperature parent β -phase.

4. Conclusions

The few-component crystallographic texture that forms in HSLA pipeline steel due to the austenite deformation and multi-path $\gamma \rightarrow \alpha$ -transformation during TMCP results from the α -phase nucleation on special CSL-boundaries (mainly $\Sigma 3$) that are formed between two main γ -phase deformation orientations from the $\{112\}\langle 111 \rangle$ combination.

The majority of austenite orientations deviate from the precise ORs (K-S, N-W and G-T) at $\sim 10^\circ$ and $\sim 20^\circ$ angles. This allows to suggest that the observed γ -phase particles are not retained austenite but are formed during the $\gamma \rightarrow \alpha \rightarrow \gamma_{II}$ -transformation, whereby

the second transformation develops on the ferrite crystallite boundaries, but corresponds to ORs (K–S, N–W and G–T) with regard to only one adjacent crystallite.

Author Contributions: Conceptualization, M.L.L. and A.A.R.; methodology, M.A.Z. and A.A.R.; data curation, M.A.Z. and M.L.L.; validation, N.V.U. and M.S.K.; investigation, M.S.K., M.L.L. and M.A.Z.; resources, N.V.U. and M.S.K.; visualization, M.A.Z.; supervision, M.L.L.; Writing—original draft, M.A.Z.; Writing—review and editing, M.L.L., A.A.R. and N.V.U. All authors have read and agreed to the published version of the manuscript.

Funding: This research was funded by the Ministry of Science and Higher Education of the Russian Federation (Ural Federal University Program of Development within the Priority-2030 Program).

Data Availability Statement: The data presented in this study are available on request from the corresponding author.

Conflicts of Interest: The authors declare no conflict of interest.

References

1. Stalheim, D.; Boggess, T.; San Marchi, C.; Jansto, S.; Somerday, B.; Muralidharan, G.; Sofronis, P. Microstructure and Mechanical Property Performance of Commercial Grade API Pipeline Steels in High Pressure Gaseous Hydrogen. In Proceedings of the 8th International Pipeline Conference, Calgary, AB, Canada, 27 September–1 October 2010.
2. Zhang, G.; Bai, X.; Stalheim, D.; Li, S.; Ding, W. Development and Production of Heavy Gauge X80 and High Strength X90 Pipeline Steels Utilizing TMCP/Optimized Cooling Process. In Proceedings of the 10th International Pipeline Conference, Calgary, AB, Canada, 29 September–3 October 2014.
3. Roccisano, A.; Nafisi, S.; Stalheim, D.; Ghomashchi, R. Effect of TMCP Rolling Schedules on the Microstructure and Performance of X70 Steel. *Mater. Charact.* **2021**, *178*, 111207. [[CrossRef](#)]
4. Lobanov, M.L.; Khotinov, V.A.; Urtsev, V.N.; Danilov, S.V.; Urtsev, N.V.; Platov, S.I.; Stepanov, S.I. Tensile Deformation and Fracture Behavior of API-5L X70 Line Pipe Steel. *Materials* **2022**, *15*, 501. [[CrossRef](#)]
5. Ray, R.K.; Jonas, J.J. Transformation Textures in Steels. *Int. Mater. Rev.* **1994**, *34*, 927–942. [[CrossRef](#)]
6. Akhtar, M.N.; Khan, M.; Khan, S.A.; Afzal, A.; Subbiah, R.; Ahmad, S.N.; Husain, M.; Butt, M.M.; Othman, A.R.; Bakar, E.A. Determination of Non-Recrystallization Temperature for Niobium Microalloyed Steel. *Materials* **2021**, *14*, 2639. [[CrossRef](#)]
7. Vervynck, S.; Verbeken, K.; Lopez, B.; Jonas, J.J. Modern HSLA Steels and Role of Non-Recrystallisation Temperature. *Int. Mater. Rev.* **2012**, *57*, 187–207. [[CrossRef](#)]
8. Inagaki, H.; Suda, T. The Development of Rolling Textures in Low-Carbon Steels. *Texture Stress Microstruct.* **1972**, *1*, 129–140. [[CrossRef](#)]
9. Inagaki, H. Transformation Textures in Control-Rolled High Tensile Strength Steels. *Trans. Iron Steel Inst. Jpn.* **1977**, *17*, 166–173. [[CrossRef](#)]
10. Yang, X.-L.; Xu, Y.-B.; Tan, X.-D.; Wu, D. Influences of Crystallography and Delamination on Anisotropy of Charpy Impact Toughness in API X100 Pipeline Steel. *Mater. Sci. Eng. A* **2014**, *607*, 53–62. [[CrossRef](#)]
11. Pyshmintsev, I.Y.; Struin, A.O.; Gervasyev, A.M.; Lobanov, M.L.; Rusakov, G.M.; Danilov, S.V.; Arabey, A.B. Effect of Bainite Crystallographic Texture on Failure of Pipe Steel Sheets Made by Controlled Thermomechanical Treatment. *Metallurgist* **2016**, *60*, 405–412. [[CrossRef](#)]
12. Lobanov, M.L.; Krasnov, M.L.; Urtsev, V.N.; Danilov, S.V.; Pastukhov, V.I. Effect of Cooling Rate on the Structure of Low-Carbon Low-Alloy Steel After Thermomechanical Controlled Processing. *Met. Sci. Heat Treat.* **2019**, *61*, 32–38. [[CrossRef](#)]
13. Kestens, L.A.I.; Nguyen-Minh, T.; Petrov, R.H. The Role of Parent Phase Topology in Double Young–Kurdjumow–Sachs Variant Selection during Phase Transformation in Low-Carbon Steels. *Metals* **2022**, *12*, 939. [[CrossRef](#)]
14. Hara, T.; Shinohara, Y.; Asahi, H.; Terada, Y. Effects of Microstructure and Texture on DWTT Properties for High Strength Line Pipe Steels. In Proceedings of the 2006 International Pipeline Conference, Calgary, AB, Canada, 25–29 September 2006; pp. 245–250.
15. Gervasyev, A.; Pyshmintsev, I.; Petrov, R.; Huo, C.; Barbaro, F. Splitting Susceptibility in Modern X80 Pipeline Steels. *Mater. Sci. Eng. A* **2020**, *772*, 138746. [[CrossRef](#)]
16. Joo, M.S.; Suh, D.-W.; Bae, J.H.; Sanchez Mouriño, N.; Petrov, R.; Kestens, L.A.I.; Bhadeshia, H.K.D.H. Experiments to Separate the Effect of Texture on Anisotropy of Pipeline Steel. *Mater. Sci. Eng. A* **2012**, *556*, 601–606. [[CrossRef](#)]
17. Hölscher, M.; Raabe, D.; Lücke, K. Relationship between Rolling Textures and Shear Textures in f.c.c. and b.c.c. Metals. *Acta Metall. Mater.* **1994**, *42*, 879–886. [[CrossRef](#)]
18. Hutchinson, B.; Ryde, L.; Lindh, E.; Tagashira, K. Texture in Hot Rolled Austenite and Resulting Transformation Products. *Mater. Sci. Eng. A* **1998**, *257*, 9–17. [[CrossRef](#)]
19. Kurdjumow, G.; Sachs, G. Über Den Mechanismus Der Stahlhärtung. *Z. Phys.* **1930**, *64*, 325–343. [[CrossRef](#)]
20. Nishiyama, Z. X-Ray Investigation of the Mechanism of the Transformation from Face-Centred Cubic Lattice to Body-Centred Cubic. *Sci. Rep. Tohoku Imp. Univ.* **1934**, *23*, 637.

21. Wassermann, G. *Ueber den Mechanismus der α - γ -Umwandlung Des Eisens*; Verlag Stahleisen: Düsseldorf, Germany, 1935.
22. Greninger, A.B.; Troiano, A.R. The Mechanism of Martensite Formation. *Jom* **1949**, *1*, 590–598. [[CrossRef](#)]
23. Kraposhin, V.; Jakovleva, I.; Karkina, L.; Nuzhny, G.; Zubkova, T.; Talis, A. Microtwinning as a Common Mechanism for the Martensitic and Pearlitic Transformations. *J. Alloys Compd.* **2013**, *577*, S30–S36. [[CrossRef](#)]
24. Sasidhar, K.N.; Dhande, T.; Javed, N.; Ghosh, A.; Mukherjee, M.; Sharma, V.; Mahashabde, V.V.; Das Bakshi, S. Effect of Transformation Texture on the Impact Toughness of Hot-Rolled Ti+Nb Microalloyed Steel. *Mater. Des.* **2017**, *128*, 86–97. [[CrossRef](#)]
25. Chang, R. An Atomistic Study of Fracture. *Int. J. Fract. Mech.* **1970**, *6*, 111–125. [[CrossRef](#)]
26. Schemmann, L.; Stallybrass, C.; Schröder, J.; Liessem, A.; Zaefferer, S. Crack Formation in Charpy Tests of the Heat-Affected Zone of Large-Diameter Linepipe Material. In Proceedings of the 12th International Pipeline Conference, Calgary, AB, Canada, 24–28 September 2018.
27. Tomida, T.; Wakita, M.; Yoshida, M.; Imai, N. Quantitative Prediction of Transformation Texture in Hot-Rolled Steel Sheets by Multiple KS Relation. In *Materials Processing and Texture*; John Wiley & Sons, Ltd.: Hoboken, NJ, USA, 2008; pp. 325–332. ISBN 978-0-470-44419-1.
28. Tomida, T.; Wakita, M. Transformation Texture in Hot-Rolled Steel Sheets and Its Quantitative Prediction. *ISIJ Int.* **2012**, *52*, 601–609. [[CrossRef](#)]
29. Gong, W.; Tomota, Y.; Adachi, Y.; Paradowska, A.M.; Kelleher, J.F.; Zhang, S.Y. Effects of Ausforming Temperature on Bainite Transformation, Microstructure and Variant Selection in Nanobainite Steel. *Acta Mater.* **2013**, *61*, 4142–4154. [[CrossRef](#)]
30. Pereloma, E.V.; Al-Harbi, F.; Gazder, A.A. The Crystallography of Carbide-Free Bainites in Thermo-Mechanically Processed Low Si Transformation-Induced Plasticity Steels. *J. Alloys Compd.* **2014**, *615*, 96–110. [[CrossRef](#)]
31. Gundyrev, V.M.; Zeldovich, V.I.; Schastlivtsev, V.M. Crystallographic Analysis and Mechanism of Martensitic Transformation in Fe Alloys. *Phys. Met. Metallogr.* **2020**, *121*, 1045–1063. [[CrossRef](#)]
32. Raabe, D. Recovery and Recrystallization: Phenomena, Physics, Models, Simulation. In *Physical Metallurgy*, 5th ed.; Laughlin, D.E., Hono, K., Eds.; Elsevier: Oxford, UK, 2014; pp. 2291–2397. ISBN 978-0-444-53770-6.
33. Andreyev, Y.G.; Zarkova, Y.I.; Shtremel, M.A. Boundaries and Subboundaries in Packet Martensite. II. Boundaries between Packets. *Fiz. Met. Metalloved.* **1990**, *69*, 169–173.
34. Lobanov, M.L.; Rusakov, G.M.; Redikul'tsev, A.A.; Belikov, S.V.; Karabanalov, M.S.; Struina, E.R.; Gervas'ev, A.M. Investigation of Special Misorientations in Lath Martensite of Low-Carbon Steel Using the Method of Orientation Microscopy. *Phys. Met. Metallogr.* **2016**, *117*, 254–259. [[CrossRef](#)]
35. Kitahara, H.; Ueji, R.; Tsuji, N.; Minamino, Y. Crystallographic Features of Lath Martensite in Low-Carbon Steel. *Acta Mater.* **2006**, *54*, 1279–1288. [[CrossRef](#)]
36. Shibata, A.; Jafarian, H.; Tsuji, N. Microstructure and Crystallographic Features of Martensite Transformed from Ultrafine-Grained Austenite in Fe–24Ni–0.3C Alloy. *Mater. Trans.* **2012**, *53*, 81–86. [[CrossRef](#)]
37. Tanaka, T. Controlled Rolling of Steel Plate and Strip. *Int. Met. Rev.* **1981**, *26*, 185–212. [[CrossRef](#)]
38. Yakovleva, I.L.; Tereshchenko, N.A.; Urtsev, N.V. Observation of the Martensitic-Austenitic Component in the Structure of Low-Carbon Low-Alloy Pipe Steel. *Phys. Met. Metallogr.* **2020**, *121*, 352–358. [[CrossRef](#)]
39. Li, X.; Fan, Y.; Ma, X.; Subramanian, S.V.; Shang, C. Influence of Martensite–Austenite Constituents Formed at Different Intercritical Temperatures on Toughness. *Mater. Des.* **2015**, *67*, 457–463. [[CrossRef](#)]
40. Platov, S.I.; Gorbatyuk, S.M.; Lobanov, M.L.; Maslennikov, K.B.; Urtsev, N.V.; Dema, R.R.; Zvyagina, E.Y. Mathematical Model of the Accelerated Cooling of Metal in Thick-Plate Hot Rolling. *Metallurgist* **2022**, *66*, 462–468. [[CrossRef](#)]
41. Erpalov, M.V.; Khotinov, V.A. Optical Method to Study Post-Necking Material Behaviour. *AIP Conf. Proc.* **2020**, *2288*, 030007. [[CrossRef](#)]
42. Huang, C.-Y.; Ni, H.-C.; Yen, H.-W. New Protocol for Orientation Reconstruction from Martensite to Austenite in Steels. *Materialia* **2020**, *9*, 100554. [[CrossRef](#)]
43. Christian, J.W. *The Theory of Transformations in Metals and Alloys*; Pergamon: Prussia, PA, USA, 2002; ISBN 0-08-044019-3.
44. Zorina, M.A.; Karabanalov, M.S.; Loginov, Y.N.; Lobanov, M.L. Crystallographic Laws of Formation of Recrystallization Texture in a Copper Capillary Tube. *Met. Sci. Heat Treat.* **2022**, *64*, 3–8. [[CrossRef](#)]
45. Пышминцев, И.Ю.; Смирнов, М.А. Структура и Свойства Сталей для Магистральных Трубопроводов; ООО Издательство УМЦ УПИ: Yekaterinburg, Russia, 2019; ISBN 978-5-8295-0659-9.
46. Rusakov, G.M.; Illarionov, A.G.; Loginov, Y.N.; Lobanov, M.L.; Redikul'tsev, A.A. Interrelation of Crystallographic Orientations of Grains in Aluminum Alloy AMg6 Under Hot Deformation and Recrystallization. *Met. Sci. Heat Treat.* **2015**, *56*, 650–655. [[CrossRef](#)]
47. Tomida, T.; Wakita, M.; Yasuyama, M.; Sugaya, S.; Tomota, Y.; Vogel, S.C. Memory Effects of Transformation Textures in Steel and Its Prediction by the Double Kurdjumov–Sachs Relation. *Acta Mater.* **2013**, *61*, 2828–2839. [[CrossRef](#)]
48. Landheer, H.; Offerman, S.E.; Petrov, R.H.; Kestens, L.A.I. The Role of Crystal Misorientations during Solid-State Nucleation of Ferrite in Austenite. *Acta Mater.* **2009**, *57*, 1486–1496. [[CrossRef](#)]
49. Lobanov, M.L.; Pastukhov, V.I.; Redikul'tsev, A.A. Effect of Special Boundaries on $\gamma \rightarrow \alpha$ Transformation in Austenitic Stainless Steel. *Phys. Met. Metallogr.* **2021**, *122*, 396–402. [[CrossRef](#)]
50. Lobanov, M.L.; Zorina, M.A.; Reznik, P.L.; Pastukhov, V.I.; Redikul'tsev, A.A.; Danilov, S.V. Specific Features of Crystallographic Texture Formation in BCC-FCC Transformation in Extruded Brass. *J. Alloys Compd.* **2021**, *882*, 160231. [[CrossRef](#)]

51. Gottstein, G. *Physical Foundation of Materials Science*; Springer: Berlin/Heidelberg, Germany, 2004; ISBN 3-540-40139-3.
52. Rollett, A.; Humphreys, F.; Rohrer, G.S.; Hatherly, M. *Recrystallization and Related Annealing Phenomena*, 2nd ed.; Elsevier Ltd.: Amsterdam, The Netherlands, 2004; ISBN 978-0-08-044164-1.
53. Ram, F.; Zaefferer, S.; Jäpel, T.; Raabe, D. Error Analysis of the Crystal Orientations and Disorientations Obtained by the Classical Electron Backscatter Diffraction Technique. *J. Appl. Crystallogr.* **2015**, *48*, 797–813. [[CrossRef](#)]
54. Lobanov, M.L.; Yarkov, V.Y.; Pastukhov, V.I.; Naschetnikova, I.A.; Stepanov, S.I.; Redikultsev, A.A.; Zorina, M.A. The Effect of Cooling Rate on Crystallographic Features of Phase Transformations in Zr-2.5Nb. *Materials* **2023**, *16*, 3758. [[CrossRef](#)]
55. Naschetnikova, I.A.; Stepanov, S.I.; Redikultsev, A.A.; Yarkov, V.Y.; Zorina, M.A.; Lobanov, M.L. Crystallographic Features of Phase Transformations during the Continuous Cooling of a Ti6Al4V Alloy from the Single-Phase β -Region. *Materials* **2022**, *15*, 5840. [[CrossRef](#)]

Disclaimer/Publisher's Note: The statements, opinions and data contained in all publications are solely those of the individual author(s) and contributor(s) and not of MDPI and/or the editor(s). MDPI and/or the editor(s) disclaim responsibility for any injury to people or property resulting from any ideas, methods, instructions or products referred to in the content.